



**HAL**  
open science

## Elastic moduli and refractive index of $\gamma$ -Ge<sub>3</sub>N<sub>4</sub>

Chen-Hui Li, Philippe Djemia, Nikolay Chigarev, Siham Sodki, Yves Roussigné, Geeth Manthilake, Franck Tessier, Samuel Raetz, Vitalyi Gusev, Andreas Zerr

► **To cite this version:**

Chen-Hui Li, Philippe Djemia, Nikolay Chigarev, Siham Sodki, Yves Roussigné, et al.. Elastic moduli and refractive index of  $\gamma$ -Ge<sub>3</sub>N<sub>4</sub>. Philosophical Transactions of the Royal Society A: Mathematical, Physical and Engineering Sciences, 2023, 381 (2258), pp.20230016. 10.1098/rsta.2023.0016 . hal-04192971

**HAL Id: hal-04192971**

**<https://hal.science/hal-04192971>**

Submitted on 12 Oct 2023

**HAL** is a multi-disciplinary open access archive for the deposit and dissemination of scientific research documents, whether they are published or not. The documents may come from teaching and research institutions in France or abroad, or from public or private research centers.

L'archive ouverte pluridisciplinaire **HAL**, est destinée au dépôt et à la diffusion de documents scientifiques de niveau recherche, publiés ou non, émanant des établissements d'enseignement et de recherche français ou étrangers, des laboratoires publics ou privés.

# Elastic moduli and refractive index of $\gamma$ -Ge<sub>3</sub>N<sub>4</sub>

Chen-Hui Li<sup>1</sup>; Philippe Djemia<sup>1</sup>; Nikolay Chigarev<sup>2</sup>; Siham Sodki<sup>1</sup>; Yves Roussigné<sup>1</sup>; Geeth Manthilake<sup>3</sup>; Franck Tessier<sup>4</sup>; Samuel Raetz<sup>2</sup>; Vitalyi E. Gusev<sup>2</sup>; Andreas Zerr<sup>1\*</sup>

<sup>1</sup> *Laboratoire des Sciences des Procédés et des Matériaux, CNRS UPR 3407, Université Sorbonne Paris Nord, F-93430 Villetaneuse, France*

<sup>2</sup> *Laboratoire d'Acoustique de l'Université du Mans, CNRS UMR 6613, Le Mans Université, F-72085 Le Mans, France;*

<sup>3</sup> *Laboratoire Magmas et Volcans, Université Clermont Auvergne, CNRS UMR 6524, Observatoire de Physique du Globe de Clermont Ferrand, F-63178 Aubière, France;*

<sup>4</sup> *Institut des Sciences Chimiques de Rennes, CNRS UMR 6226, Université Rennes, F-35000 Rennes, France.*

**Keywords:** spinel nitrides, elastic moduli, optical properties, laser ultrasonics, Brillouin light scattering, first-principles calculations

Germanium nitride having cubic spinel structure,  $\gamma$ -Ge<sub>3</sub>N<sub>4</sub>, is a wide band-gap semiconductor with a large exciton binding energy which exhibits high hardness, elastic moduli and elevated thermal stability up to  $\sim 700^\circ\text{C}$ . Experimental data on its bulk and shear moduli ( $B_0$  and  $G_0$ , respectively) are strongly limited, inconsistent and, thus, require verification. Moreover, earlier first-principles density functional calculations provided significantly scattering  $B_0$  values but consistently predicted  $G_0$  much higher than the so far available experimental value. Here, we examined the elasticity of polycrystalline  $\gamma$ -Ge<sub>3</sub>N<sub>4</sub>, densified applying high pressures and temperatures, using the techniques of laser ultrasonics (LU) and Brillouin light scattering (BLS) and compared with our extended first-principles calculations. From the LU measurements, we obtained its longitudinal- and Rayleigh wave sound velocities and, taking into account the sample porosity, derived  $B_0=322(44)$  GPa and  $G_0=188(7)$  GPa for the dense polycrystalline  $\gamma$ -Ge<sub>3</sub>N<sub>4</sub>. While our calculations underestimated  $B_0$  by  $\sim 17\%$ , most of the predicted  $G_0$  matched well our experimental value. Combining the LU- and BLS data and taking into account the elastic anisotropy, we determined the refractive index of  $\gamma$ -Ge<sub>3</sub>N<sub>4</sub> in the visible range of light to be  $n=2.4$ , similarly high as that of diamond or GaN, and matching our calculated value.

## 1 Introduction

$\gamma$ -Ge<sub>3</sub>N<sub>4</sub> was independently discovered by two research teams, one from Arizona State University (ASU) [1, 2] and other from Max-Planck Institute for Chemistry in Mainz and Technical University Darmstadt [3], in 1999. Paul McMillan participated in this work as a member of the ASU team and continued to study this and other phases of Ge<sub>3</sub>N<sub>4</sub> when he moved to University College London. Today, we know that  $\gamma$ -Ge<sub>3</sub>N<sub>4</sub> is a multifunctional material exhibiting a wide and direct electronic band gap of  $E_g=3.65(5)$  eV combined with a large exciton binding energy,  $D_e$ , between 170 and 300 meV [4, 5], high elastic moduli (**Tables 1 and 2**) and hardness. It is thermodynamically stable at pressures above 10 GPa but recoverable at ambient conditions [2, 3, 6] and persists heating to  $\sim 700^\circ\text{C}$  [7]. In contrast to the low-pressure hexagonal phases with four-fold coordinated cations,  $\alpha$ - and  $\beta$ -Ge<sub>3</sub>N<sub>4</sub>, 2/3 of all Ge-cations in  $\gamma$ -Ge<sub>3</sub>N<sub>4</sub> are six-fold coordinated. This increase of the coordination number leads to a 25% higher density of  $\gamma$ -Ge<sub>3</sub>N<sub>4</sub> ( $\rho_{\gamma,0}=6.585$  g/cm<sup>3</sup> at atmospheric pressure, see below) when compared with the  $\alpha$ - and  $\beta$ -phases having almost identical densities of  $\rho_{\alpha,0}=5.254$  g/cm<sup>3</sup> and  $\rho_{\beta,0}=5.287$  g/cm<sup>3</sup>, respectively [8]. (Here and below, the subscript 0 indicates values for pore-free materials at ambient conditions). The higher density and cation coordination number resulted in advanced mechanical properties of  $\gamma$ -Ge<sub>3</sub>N<sub>4</sub>: Its Vickers hardness,  $H_V$ , measured to be between 23 and 33 GPa [9] is comparable with that of the well-known ceramics  $\alpha$ - or  $\beta$ -Si<sub>3</sub>N<sub>4</sub> (31 GPa and 20 GPa, respectively) or  $\beta$ -SiC (23GPa) e.g.[10]. Empirical and theoretical works predicted, however, significantly lower  $H_V$  between 18 and 24 GPa [11-13].  $\gamma$ -Ge<sub>3</sub>N<sub>4</sub> was also found to

exhibit a high fracture toughness of  $K_{IC} \approx 2.3 \text{ MPa}\cdot\text{m}^{1/2}$ , similar to that of sapphire [9]. Despite the advancement in examination of its properties, previous experimental and theoretical reports on elastic moduli of  $\gamma\text{-Ge}_3\text{N}_4$  are inconsistent: The so-far measured equations of state (EOSs),  $\rho(P)$ , provided very different values of its bulk modulus of  $B_0=295(5) \text{ GPa}$  [1] and  $B_0=254(13) \text{ GPa}$  [6] (**Table 1**). Earlier first-principles calculations based on the density functional theory (DFT) predicted  $B_0$ -values significantly below the experimental  $B_0=295 \text{ GPa}$  independent of the applied density functionals, local-density approximation (LDA) or generalized-gradient approximation (GGA) [9, 11, 15-20] (**Table 2**). The only existing experimental value of shear modulus of  $G_0=124\text{-}129 \text{ GPa}$  (**Table 1**), derived from nanoindentation testing (NIT) [9, 14], is much lower than all so-far predicted values, between 169 GPa and 176 GPa (**Table 2**). Thus, independent measurements of  $B_0$  and  $G_0$  of  $\gamma\text{-Ge}_3\text{N}_4$  are essential for the understanding of sources of the differences between the calculated and experimental values. Also, such data are useful by establishing relationships between elastic moduli and hardness of a large variety of materials, in general, e.g. Ref. [21] or within the family of spinel nitrides,  $\gamma\text{-M}_3\text{N}_4$  where  $M=\text{Si, Ge, or Sn}$  [13, 22].

**Table 1:** Experimental  $B_0$  and  $G_0$  of polycrystalline  $\gamma\text{-Ge}_3\text{N}_4$  and its cubic lattice parameter,  $a_0$ . Applied experimental methods such as LU, NIT or EOS (including the used PTM) are indicated.

$B_0$ (GPa)	$G_0$ (GPa)	$a_0$ (Å)	Method	References
322(44)	188(7)	8.2048(6)	LU	this work
295(5)	-	8.2125(1)	EOS (PTM: Ar)	[1, 2]
-	124 <sup>a</sup>	-	NIT	[9, 14]
-	129 <sup>b</sup>	-	NIT	[9, 14]
254(13)	-	-	EOS (PTM: MgO)	[6]

<sup>a</sup> derived from NIT of a polycrystalline sample of  $\gamma\text{-Ge}_3\text{N}_4$  with unknown porosity using the experimental  $B_0=295 \text{ GPa}$  reported in [1]; <sup>b</sup> derived from NIT of a polycrystalline sample of  $\gamma\text{-Ge}_3\text{N}_4$  with unknown porosity using the theoretical  $B_0=260 \text{ GPa}$  calculated in the same work.

As mentioned above,  $\gamma\text{-Ge}_3\text{N}_4$  exhibits not only advanced mechanical properties but also promising optoelectronic properties: Its wide and direct band gap combined with the large exciton binding energy makes  $\gamma\text{-Ge}_3\text{N}_4$  suitable for fabrication of UV-LEDs with a very high efficiency of conversion of electric energy to light, also at very high temperatures [4, 5]. This makes  $\gamma\text{-Ge}_3\text{N}_4$  advantageous when compared with GaN, which has a similar band gap of  $E_g=3.39 \text{ eV}$  but much lower  $D_e=26 \text{ meV}$  [23, 24], because the ratio  $D_e/T$  defines the energy conversion efficiency in a LED [4, 25]. It is also expected that  $\gamma\text{-Ge}_3\text{N}_4$  exhibits, as earlier proposed for oxidic compounds having spinel structure (e.g.,  $\text{MgAl}_2\text{O}_4$ ), a high tolerance to irradiation with energetic particles due to a large number of structural vacancies in the cation sub-lattice [26, 27].

In this work, we synthesised a macroscopic sample of polycrystalline  $\gamma\text{-Ge}_3\text{N}_4$  at high pressures and temperatures and measured its bulk and shear moduli using the technique of laser ultrasonics (LU) providing velocities of the bulk longitudinal waves (LWs) and Rayleigh surface waves (RWs). Because our  $\gamma\text{-Ge}_3\text{N}_4$  sample was not fully densified, the measured bulk and shear moduli ( $B_p$  and  $G_p$ , respectively) were affected by the porosity,  $p$ . (Here and below, the subscript p indicates values for the porous sample.) Applying the Hashin-Shtrikman approach, we derived  $B_0$  and  $G_0$  of  $\gamma\text{-Ge}_3\text{N}_4$  using the measured  $B_p$ ,  $G_p$  and  $p$  [28]. This approach was already demonstrated to deliver reliable elastic moduli of dense materials using the data for porous samples: In earlier experiments on transition metal nitrides,  $B_0$ -values derived from such LU measurements [28, 29] agreed very well with those obtained from X-ray diffraction (XRD) measurements of the unit cell volume on quasihydrostatic compression [30, 31], which is, by definition, an EOS of a perfectly densified material. We also examined the same  $\gamma\text{-Ge}_3\text{N}_4$  sample using Brillouin light spectroscopy (BLS). Comparison of the BLS- and LU data revealed a difference in the RW velocity,  $V_R$ , which we attributed to the elastic anisotropy of  $\gamma\text{-Ge}_3\text{N}_4$ . Combining the LU- and BLS data we derived a very high refractive index,  $n$ , of  $\gamma\text{-Ge}_3\text{N}_4$ . The LU- and BLS measurements were accompanied by first-principles calculations of the single crystal elastic moduli  $C_{ij}$  (accessible today only theoretically), cubic lattice parameter  $a_0$  (**Table 2**), and refractive index of  $\gamma\text{-Ge}_3\text{N}_4$ . Comparison with the experimental data

permitted identification of the most suitable density functional and pseudopotential for the calculation of the elastic and optical properties of  $\gamma$ -Ge<sub>3</sub>N<sub>4</sub>.

**Table 2:** Single-crystal elastic moduli  $C_{ij}$ ,  $B_0$ ,  $G_0$  (derived from the  $C_{ij}$  values using the Hill approximation), and  $a_0$  of  $\gamma$ -Ge<sub>3</sub>N<sub>4</sub> predicted using DFT involving either the local-density approximation (LDA) or the generalized-gradient approximation (GGA). In the latter case, applied functionals, if mentioned, are indicated. Choices of projector augmented wave (PAW) pseudopotentials include standard ones, as well as a hard one indicated notably by  $-h$ . Zener ratios,  $A = 2 \cdot C_{44} / (C_{11} - C_{12})$ , used to quantify elastic anisotropy of cubic solids are also given.

$C_{11}$ (GPa)	$C_{12}$ (GPa)	$C_{44}$ (GPa)	$B_0$ (GPa)	$G_0$ (GPa)	$a_0$ (Å)	$A$	Methods	References
346	143	201	211	153(8)	8.309	1.98	GGA-PBE	this work
377	160	226	232	169(10)	8.228	2.08	GGA-PBEsol	this work
435	184	241	267	186(10)	8.207	1.92	GGA-PBEsol- $h$	this work
387	178	214	248	160(10)	8.196	2.05	META-GGA	this work
431	170	248	257	192(10)	8.204	1.91	HSE06+PBE- $h$	this work
402	168	235	246	178(10)	8.178	2.01	LDA	this work
392	159	232	237	176(10)	8.204 <sup>a</sup>	1.99	LDA	this work
368	146	223	220	169	8.288	2.01	GGA-PBE	[15]
387	151	224	230	173	8.267	1.90	GGA	[16]
-	-	-	208	-	8.313	-	GGA	[17]
-	-	-	237	-	8.34	-	GGA-PBE	[18]
395	165	235	242	176	8.168	2.04	LDA	[11]
-	-	-	269	-	8.211	-	LDA	[19]
-	-	-	260	-	8.18	-	LDA	[9]
-	-	-	266	-	8.12	-	-	[20]

<sup>a</sup> cubic lattice parameter was fixed to be equal to our experimental value (s. **Table 1**)

## 2 Methods

### 2.1 Experiment

The examined sample of polycrystalline  $\gamma$ -Ge<sub>3</sub>N<sub>4</sub> was synthesized at high pressures and temperatures in a multi-anvil press following the earlier developed procedure [2]: Powder of  $\beta$ -Ge<sub>3</sub>N<sub>4</sub>, used as the starting material, was prepared via a reaction of GeO<sub>2</sub> with flowing ammonia heated in a tubular furnace to 880°C during 12h. The product was annealed under the same conditions for purity purpose and the phase composition was identified by XRD to be pure  $\beta$ -Ge<sub>3</sub>N<sub>4</sub>. Elemental analyses, performed using a Leco TC-600 analyser, showed a low level of oxygen contamination of ~0.3 wt%. No traces of carbon, eventually coming from the synthesis route or from the used vessels, were found. The  $\beta$ -Ge<sub>3</sub>N<sub>4</sub> powder, compacted in a graphite capsule, was placed in a multi-anvil press, compressed to ~13 GPa and heated to 1200 °C for 20 min. The recovered monolithic sample of  $\gamma$ -Ge<sub>3</sub>N<sub>4</sub> was a cylinder of ~0.5 mm in diameter and ~1 mm in height exhibiting a low but not neglectable porosity. It was opaque but the cleaved thin slices were translucent. The sample was first examined using powder XRD and Raman spectroscopy. The XRD patterns were obtained applying a set-up consisting of a micro-focus source delivering Mo- $K\alpha$  radiation focused to a spot of less than 200  $\mu$ m in diameter (I $\mu$ S high Brilliance-Incoatec Microfocus Source Mo ELM33, Incoatec) and an imaging plate detector with online readout system (mar345, marXperts). The collected 2D patterns were converted to standard diffractograms  $I(2\theta)$  using the Fit2D software [32]. In order to maximize the statistics and thus detect possible minor amounts of admixtures, the XRD measurements were performed in grazing geometry with the incidence angle of ~7°. This approach permitted detection of potential contaminating phases (e.g. remains of the starting  $\beta$ -Ge<sub>3</sub>N<sub>4</sub> or GeO<sub>2</sub>) in amounts as small as 0.5 vol.% but none were recognised. Using the XRD patterns we derived the cubic lattice parameter of our  $\gamma$ -Ge<sub>3</sub>N<sub>4</sub> to be  $a_0=8.2048(6)$  Å, slightly below the earlier  $a_0=8.2125(1)$  Å [1, 2]. Applying our  $a_0$ -value, we calculated density of the pores-free  $\gamma$ -Ge<sub>3</sub>N<sub>4</sub> to be  $\rho_0=6.585$  g/cm<sup>3</sup>. Raman spectra were excited using a He-Ne laser ( $\lambda=632.78$  nm) and recorded with a Jobin Yvon HR800 spectrometer (spectral resolution ~1 cm<sup>-1</sup>) equipped with a Peltier cooled CCD detector. The spectra

showed presence of only one compound with Raman-active modes, namely  $\gamma$ -Ge<sub>3</sub>N<sub>4</sub>, similar to those described earlier [33].

After the above characterisation, the sample was embedded in epoxy and polished using diamond abrasives with grain sizes successively reducing from 30  $\mu\text{m}$  down to 0.25  $\mu\text{m}$  until a mirror-quality surface finish was obtained. This was needed to determine the elemental composition by means of the electron probe microanalysis (EPMA) and to measure velocities of LWs and RWs ( $V_L$  and  $V_R$ , respectively) applying the LU- and BLS techniques described below. The EPMA was performed using a Cameca SxFiveTactis electron microprobe, installed at the LMV, operating at an accelerating voltage of 15 kV and a beam current of 20 nA. In order to verify chemical homogeneity of the sample, the elemental composition was measured in 10 points along a line, from one sample edge to the opposite. The sample was found to be chemically homogeneous and the average composition to be 79.7 wt.% for Ge, 19.6 wt.% for N, and 1.3 wt.% for O. The sum of the three elements of 100.6 wt.% indicated that no other element was present in our product in detectable amounts. The normalised elemental composition was calculated to be 42.6 at.%, 54.3 at.% and 3.1 at.%, respectively. The standard deviation of the measurement for each of the elements was typically  $\sim 0.6\%$  for Ge,  $\sim 3.5\%$  for N and  $\sim 8.3\%$  for O. Interestingly, the elements ratio O:(N+O)=5.4% obtained for our  $\gamma$ -Ge<sub>3</sub>N<sub>4</sub> was below the ratios O:(N+O)=5.6% and O:(N+O)=6.9% reported in the works on the high-pressure multianvil synthesis of  $\gamma$ -Si<sub>3</sub>N<sub>4</sub> where special precautions were undertaken to minimize the possible sample oxidation [34, 35]. Thus, the used here graphite capsule provided an effective barrier against the diffusion of oxygen from the oxide components of the multianvil assembly into the sample volume. Finally, the obtained elemental composition suggested that 5.4% of the anion positions in the spinel structure were occupied by oxygen because the amount of oxygen and nitrogen in our product, (O+N)=57.4 at.%, was almost identical to the amount of anions in an ideal binary compound having spinel structure, namely 57.1 at.%. However, the presence of a minor amount of a (partially) oxidised amorphous material between the  $\gamma$ -Ge<sub>3</sub>N<sub>4</sub> grains could not be ruled out.

To measure  $V_{L,p}$  and  $V_{R,p}$  in our  $\gamma$ -Ge<sub>3</sub>N<sub>4</sub> sample, we applied the LU set-up described in detail elsewhere [28, 29]. In this set-up, suitable for the measurement of sound velocities on surfaces as small as  $\sim 150 \mu\text{m}$ , acoustic pulses were excited with pulsed radiation of a Nd:YAG-laser (Teem Photonics,  $\lambda_L=1064 \text{ nm}$ , pulse duration 0.75 ns, pulse energy 70  $\mu\text{J}$ , repetition frequency 1 kHz) focused to a  $5 \mu\text{m} \times 100 \mu\text{m}$  line by an objective (NACHET,  $\times 20$ ) and a cylindrical lens in front of the latter. The maximal pump-laser power was limited by the ablation of the sample material whose traces can be recognised in **Figure 1a**. Arrivals of the acoustic pulses at a distance  $d$  from the pump-laser spot were detected using a probe laser beam (Coherent, Verdi 2W,  $\lambda=532 \text{ nm}$ , cw power  $\sim 50 \text{ mW}$ ) focused to a spot of 5  $\mu\text{m}$  in diameter. The arrival time of the acoustic pulses,  $t$ , was determined applying the knife-edge method which recorded deflection of the probe-laser beam (reflected from the sample surface) when the pulses passed through the probe-laser spot (**Figure 2**). For each time  $t$ , determined using an oscilloscope (LeCroy SDA18000, 18 GHz bandwidth), we derived duration of propagation of the acoustic pulses,  $\Delta t$ , through the distance  $d$ . The latter was changed by a calibrated positioning system in steps of 5.35  $\mu\text{m}$ .

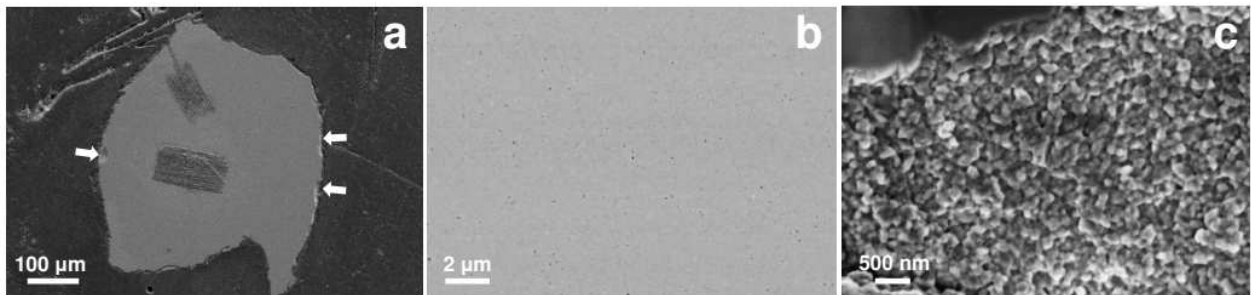


**Figure 1.** SEM images of our  $\gamma$ -Ge<sub>3</sub>N<sub>4</sub> sample: (a) Polished surface of the entire sample after the LU measurements showing traces of the material ablation caused by the pump laser. White arrows indicate fractured edges of the sample where the material grains could be recognised and their sizes evaluated (see (c)). (b) Image of the sample area collected with a higher magnification where nearly circular pores with diameters below  $\sim 0.2 \mu\text{m}$  can be recognised; (c) Image of a fractured sample edge, collected with a high magnification, showing grains of the examined material.

Afterwards, high-resolution images were collected around the areas of the LU-measurements using a scanning electron microscope (SEM, Zeiss, SUPRA 40VP, resolution 2 nm at the voltage of 3 kV) in order to determine the sample porosity (**Figure 1**). Images of the unaffected polished parts of the sample surface, coated with a thin carbon film, revealed a minor amount of nearly circular pores (recognised as dark areas exhibiting very low signal intensities) with diameters below  $\sim 0.2 \mu\text{m}$  distributed throughout the whole sample surface (**Figure 1b**). In order to determine the sample porosity, we applied a numerical approach based on the threshold filtering of pixels with the low signal intensities. Such analysis of several SEM images provided the average sample porosity of  $p=0.026(3)$  where the number in brackets indicates the standard deviation. This porosity value we used to derive elastic moduli of dense  $\gamma\text{-Ge}_3\text{N}_4$  (with  $p=0$ ) from the sound velocities  $V_{L,p}$  and  $V_{R,p}$  measured for our porous sample. SEM images of fractured sample edges showed grains of  $\gamma\text{-Ge}_3\text{N}_4$  having sizes between  $0.1\text{-}0.3 \mu\text{m}$  (**Figure 1c**). Because the grains were much smaller than the characteristic distances in our LU-measurements (**Figure 1a**), the elastic response of our sample (e.g., sound velocities) could be regarded as that of an isotropic polycrystalline material, as required in the Hill approximation used to derive  $G_0$  from  $C_{ij}$  values [36].

Finally, we applied the classical BLS technique to measure intensities of laser radiation scattered by the LWs and RWs of  $\gamma\text{-Ge}_3\text{N}_4$ . The sample was irradiated with a solid-state Nd:YAG laser beam (Laser Quantum,  $\lambda_0=532 \text{ nm}$ ) focused to a spot of  $\sim 70 \mu\text{m}$  in diameter. The BLS-spectra were recorded using the tandem  $2\times 3$  pass spectrometer [37, 38]. The measurements were performed in the backscattering geometry where direction of the incident laser radiation was opposite to that of the scattered one, ( $\chi_i = -\chi_s$ ). In this geometry, we detected peaks corresponding to the bulk LWs propagating nearly perpendicular to the sample surface as well as to the RWs propagating parallel to the surface. In the latter case, the BLS spectra were collected at various incidence angles of the primary beam ( $\theta$ ) in order to confirm the nature of the scattering acoustic waves.

## 2.2 First-principles calculations

The calculations were performed using the projector augmented wave (PAW) method as implemented in the Vienna Ab-initio Simulation Package (VASP) [MedeA-VASP, VASP license LSPM-CNRS-Université Paris 13]. Besides the application of standard (soft) PAW potentials, we used a hard version [39] which requires high cutoff energies and yields higher accuracy of the total energy. Various exchange-correlation functionals including the Perdew-Burke-Ernzerhof (PBE) or that revised for solids (PBEsol) [40] generalized gradient approximation (GGA) and the local density approximation (LDA) were used [39, 41, 42] together with the META-GGA RevTPSS functional [43]. Plane wave cut-off energy of  $520\text{-}980 \text{ eV}$ , depending on the pseudopotentials, and  $27\times 27\times 27$   $k$ -point mesh centred on the gamma point, which corresponds to actual  $k$ -spacings of  $0.049\times 0.049\times 0.049$  per Angstrom, were chosen. The electronic iteration convergence criterion was fixed at  $10^{-6} \text{ eV}$  and the force criterion at  $0.01 \text{ eV}/\text{\AA}$  for relaxation. The elastic constants were calculated using the stress-strain method [44]. By applying appropriate strains,  $\varepsilon_{ij}$ , in the range  $\pm 0.1\text{-}0.5\%$ , as implemented in Materials Exploration and Design Analysis (MedeA) software [45] and VASP, the relaxed cells were deformed, the corresponding stresses,  $\sigma_{ij}$ , calculated and the stiffness tensor  $C_{ij}$  derived using the Hooke's law. It should be mentioned here that a less dense  $k$ -spacing of  $0.188\times 0.188\times 0.188$  per Angstrom was applied by calculation of the elastic properties of  $\gamma\text{-Ge}_3\text{N}_4$  using the HSE06 functional in order to accelerate their processing. In this case, the elastic constants were obtained with the uncertainty of 3 GPa.

Wavelength dependent optical properties such as permittivity function,  $\varepsilon=\varepsilon_1-i\cdot\varepsilon_2$ , and refractive index,  $N=n-i\cdot\kappa$ , were calculated using only one of the functionals applied above to calculate the stiffness tensor, namely the hybrid functional HSE06 [46]. This functional was reported to provide, for multiple insulating systems, band gaps well comparable to the experimental ones [47, 48], even with a less-demanding  $k$ -point sampling of the Brillouin zone [49]. The exchange-correlation energy for the HSE06 functional is given by  $E_{XC}^{HSE}(\alpha;\mu)$ , where  $\alpha$  stands for the Hartree-Fock (HF) mixing parameter which defines the fraction of exact exchange in a hybrid functional calculation, and  $\mu$  stands for the screening parameter which specifies the separation range where the HF exchange is calculated. The original parameterization utilized  $\alpha=0.25$  and  $\mu=0.2 \text{ \AA}^{-1}$ . With such parameterization, the HSE06 functional provided the ground state lattice parameter  $a_0=8.204 \text{ \AA}$  (**Table 2**) and electronic band gap energy  $E_g=3.44 \text{ eV}$  for  $\gamma\text{-Ge}_3\text{N}_4$ ,

close to the experimental value of  $E_g=3.65(5)$  eV [4, 5]. In our optical property calculations, the complex shift used to smooth the real part of the dielectric function was set to 0.1.

### 3 Results and Discussion

In our LU measurements, propagation of the acoustic pulses was measured for the pump-probe distances  $d$  between  $\sim 19$   $\mu\text{m}$  and  $\sim 67$   $\mu\text{m}$ . We could recognize strong signals due to the arrivals of the RWs, and weak signals due to the skimming LWs whose amplitude decreased rapidly with  $d$  (**Figure 2a**). The LWs signals could not be improved above the shown level because further increase of the pump-pulse energy only resulted in a stronger ablation of the sample material (see **Figure 1a**). Linear fits to these two sets of the experimental data-points,  $d(\Delta t)$ , provided velocities of the both acoustic waves (**Figure 2b**): For the RWs and LWs, we measured  $V_{R,p}=4.87(5)$  km/s and  $V_{L,p}=9.2(3)$  km/s, respectively. From these values, applying the well-known equation [50]

$$\left(V_T^2 - \frac{V_R^2}{2}\right)^2 = \frac{V_T^3}{V_L} \sqrt{V_L^2 - V_R^2} \sqrt{V_T^2 - V_R^2}, \quad (1)$$

we derived velocity of the transversal sound waves (TWS) to be  $V_{T,p}=5.29(8)$  km/s. The values of  $V_{T,p}$  and  $V_{L,p}$  were subsequently used to obtain  $B_p=304(43)$  GPa and  $G_p=179(6)$  GPa for our polycrystalline sample of  $\gamma\text{-Ge}_3\text{N}_4$  having a low but not neglectable porosity. Here, we applied the well-known relationships between the sound velocities, elastic moduli and density [50]:

$$V_T = (G/\rho)^{1/2}; V_L = ((3 \cdot B + 4 \cdot G)/(3 \cdot \rho))^{1/2} \quad (2)$$

In this equation, the sample density  $\rho_p=6.414$  g/cm<sup>3</sup> was determined using the expression  $\rho_p = (1-p) \cdot \rho_0$ , where  $p=0.026(3)$  and  $\rho_0=6.585$  g/cm<sup>3</sup> were obtained in the above-described SEM- and XRD measurements, respectively. Subsequently, Poisson's ratio and Young's modulus of our porous  $\gamma\text{-Ge}_3\text{N}_4$  were found to be  $\nu_p=0.25(3)$  and  $E_p=450(18)$  GPa, respectively. In order to derive elastic moduli of the dense  $\gamma\text{-Ge}_3\text{N}_4$  ( $B_0$ ,  $G_0$ ,  $\nu_0$ , and  $E_0$ ) from the experimental  $B_p$ ,  $G_p$ ,  $\nu_p$ , and  $E_p$ , we applied the Hashin-Shtrikman approach as described earlier in Refs.[28, 51]:

$$B_p = \frac{(1-p)B_0}{1+p(3B_0/4G_0)} \quad (3a)$$

$$G_p = \frac{(1-p)G_0}{1+p(8-10\nu_0)/(7-5\nu_0)} \quad (3b)$$

and obtained  $B_0=322(44)$  GPa,  $G_0=188(7)$  GPa,  $\nu_0=0.25(4)$  and  $E_0=472(19)$  GPa. Using these moduli, we calculated  $V_{L,0}=9.3(4)$  km/s,  $V_{R,0}=4.92(10)$  km/s, and  $V_{T,0}=5.34(9)$  km/s for the dense  $\gamma\text{-Ge}_3\text{N}_4$  ( $p=0$ ).

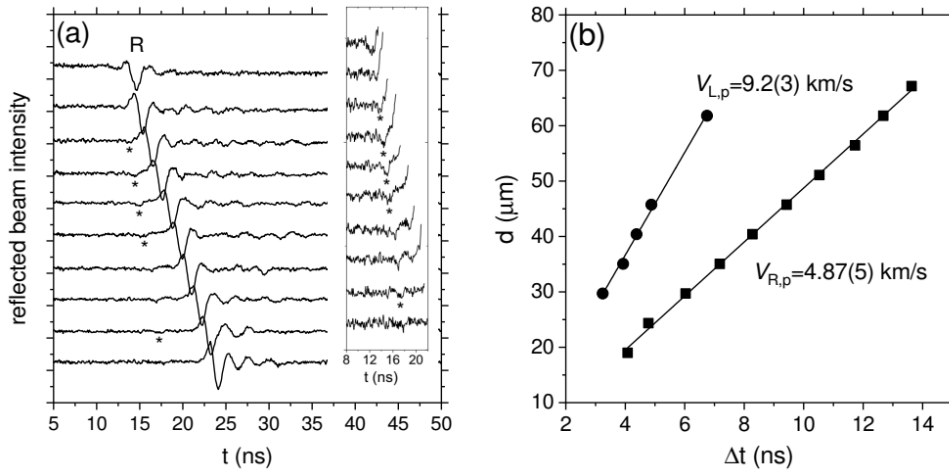


**Figure 2.** (a) Photoacoustic signals recorded for our polycrystalline sample of  $\gamma\text{-Ge}_3\text{N}_4$  when the pump-probe distance  $d$  changed from  $\sim 19$   $\mu\text{m}$  (upper signal) to  $\sim 67$   $\mu\text{m}$  in steps of  $5.35$   $\mu\text{m}$ . The signals were dominated by arrivals of the RWs but those of the skimming LWs (indicated by \*) were also detected. The insert shows arrivals of the LWs with a higher magnification. (b) Distance of propagation of the LWs (circles) and of the RWs (squares),  $d$ , as a function of the needed time  $\Delta t$ . Solid lines show linear fits to the experimental data-points. Their slopes provided the experimental values of  $V_{L,p}$  and  $V_{R,p}$ , respectively.

Our experimental  $B_0=322(44)$  GPa agrees, within the experimental uncertainties, with the earlier  $B_0=295(5)$  GPa derived from the equation of state (EOS),  $\rho(P)$ , reliably measured upon quasi-hydrostatic compression of a powder sample to 40 GPa [1] (**Table 1**). In that work, the quasi-hydrostatic compression was insured by use of solid argon as a pressure transmitting medium (PTM) confirmed experimentally to be very soft [52, 53]. Our experimental  $B_0$  disproves the much lower  $B_0=254(13)$  GPa derived from only four  $\rho(P)$ -data-points obtained upon nonhydrostatic compression to 90 GPa in a rigid PTM, namely MgO [6] (**Table 1**). As a result, these  $\rho(P)$ -data-points scattered stronger than the stated experimental uncertainties. All previous and present calculations predicted lower  $B_0$ , independent of the used functional (**Table 2**). However, the difference is less dramatic for the earlier LDA calculations reporting  $B_0=260$ -269 GPa [9, 19, 20] and for our calculations based on the GGA-PBEsol functional combined with the hard PAW pseudopotential [39] which provided  $B_0=267$  GPa.

Our experimental  $G_0=188(7)$  GPa exceeds by 33% the  $G_0=124$ -129 GPa derived from the earlier NIT [9, 14]. The discrepancy cannot be explained by the application of the two different techniques because the earlier LU- and NIT measurements on one and the same porous sample of another high-pressure binary nitride, namely  $\eta$ -Ta<sub>2</sub>N<sub>3</sub>, provided similar results: The NITs led to the reduced elastic modulus  $E_{r,p}=222(6)$  GPa [54], similar to  $E_{r,p}=201(10)$  GPa recovered from the analogous LU measurements [29]. However, inconsistencies in treatment of the NIT data in Ref. [9] were noticed in the literature [14]. A higher oxygen content in the sample of Shemkunas et al. [9], reported to be  $\sim 3$  wt.% (corresponds to O:(O+N) $\sim 12.5\%$ ), could be responsible for the recognised here discrepancy in the  $G_0$  values even though the oxygen content appears to be moderately higher than that in our sample, 1.3 wt.% (corresponds to O:(O+N)= 5.4%). It is known from the literature that a similarly moderate increase of the O:(O+N) ratio in other nitride having spinel structure, namely  $\gamma$ -Si<sub>3</sub>N<sub>4</sub>, caused a significant change of the elastic moduli [35, 55]. In particular,  $G_0=148(16)$  GPa was reported for the  $\gamma$ -Si<sub>3</sub>N<sub>4</sub> sample with O:(O+N)=9% (corresponds to the reported 4 wt.%) [55] while  $G_0=248(1)$  GPa was measured for another  $\gamma$ -Si<sub>3</sub>N<sub>4</sub> sample with O:(O+N)=5.5% (corresponds to the reported 2.5 wt.%) [35]. This reduction of  $G_0$  of  $\gamma$ -Si<sub>3</sub>N<sub>4</sub> by 40% is even higher than the 33% reduction we recognised for  $\gamma$ -Ge<sub>3</sub>N<sub>4</sub>. However, a significant porosity in the former  $\gamma$ -Si<sub>3</sub>N<sub>4</sub> sample, not evaluated in that earlier work [55], could also contribute to the much stronger decrease in  $G_0$  when compared with our observation for  $\gamma$ -Ge<sub>3</sub>N<sub>4</sub>.

All calculations, except those based on the Meta-GGA- and GGA-PBE functionals, predicted  $G_0$  similar to our experimental  $G_0=188(7)$  GPa (**Table 2**). As above for  $B_0$ , the GGA-PBEsol functional with hard pseudopotential provided  $G_0=186(10)$  GPa perfectly matching our experimental result, as is also the case for the predicted and measured,  $a_0=8.207$  Å and  $a_0=8.2048(6)$  Å, respectively. We note that the hybrid functional HSE06 also predicted  $a_0=8.204$  (Å) and  $G_0=192(10)$  GPa in close agreement with the experimental values. However, the predicted  $B_0=257$  GPa is below our and the previous [1] experimental values, as is the case for all considered here exchange-correlation functionals.

We also performed classical BLS measurements on the same  $\gamma$ -Ge<sub>3</sub>N<sub>4</sub> sample (**Figure 3a and 3b**) in order to compare the obtained sound velocities with those from our LU measurements and to recover the refractive index  $n$  of  $\gamma$ -Ge<sub>3</sub>N<sub>4</sub>. In the low-frequency range, between 5 GHz and 20 GHz, we detected a weak BLS peak corresponding to the RWs (**Figure 3a**) whose  $V_R$  can be derived from the peak frequency  $f_R$  without knowledge of the refractive index:

$$f_R = V_R \cdot 2 \cdot \sin\theta / \lambda_0 \quad (4)$$

where  $\theta$  is the angle of incidence of the exciting laser beam with  $\lambda_0=532$  nm. Thus, the  $V_R$  value obtained in the BLS measurements can be directly compared with that from the above described LU measurements. Our BLS spectra, collected for several angles  $\theta$ , resulted in the  $V_R=4.42(3)$  km/s which is  $\sim 10\%$  below the  $V_{R,0}=4.92(10)$  km/s we obtained using the LU technique. The difference can be explained by an asymmetric distribution of the scattered intensity in the BLS-peak collected from our polycrystalline samples of  $\gamma$ -Ge<sub>3</sub>N<sub>4</sub> exhibiting a significant elastic anisotropy (**Table 2**). Asymmetry of BLS-peaks collected from polycrystalline samples of elastically anisotropic cubic solids and its influence on the recovered sound velocities was experimentally revealed and theoretically validated for LWs and TWs [53, 56, 57]. In the most recent work, the occurrence frequency of all possible  $V_L$  values in texture-free

polycrystalline samples of NaCl and solid argon was analysed and a remarkable and predictable asymmetry of the collected BLS peaks found. In particular, histograms representing the occurrence frequency of all possible  $V_L$  values exhibited maxima at  $V_{L(110)}$ , the LW velocity in a single crystal along the crystallographic direction  $\langle 110 \rangle$  which is much closer to  $V_{L(111)}$  than to  $V_{L(100)}$  [57]. We note that the latter two values represent the extremes of  $V_L$  in any cubic single crystal. In the case of TWs, the tendency is similar but the  $V_T$  histograms are much broader and not uniform [57]. Because the histograms represent distribution of the BLS peak intensity, their asymmetry should be detectable in BLS measurements provided the signal-to-noise ratio is high. However, the opposite is typical for this experimental technique because accurate shapes of the BLS peaks collected from polycrystalline solids require an unacceptably long counting. As a result,  $V_L$  and  $V_T$  derived from such BLS peaks are overestimated if the Zener anisotropy ratio  $A$  exceeds unity, as is the case for  $\gamma$ -Ge<sub>3</sub>N<sub>4</sub> (**Table 2**).

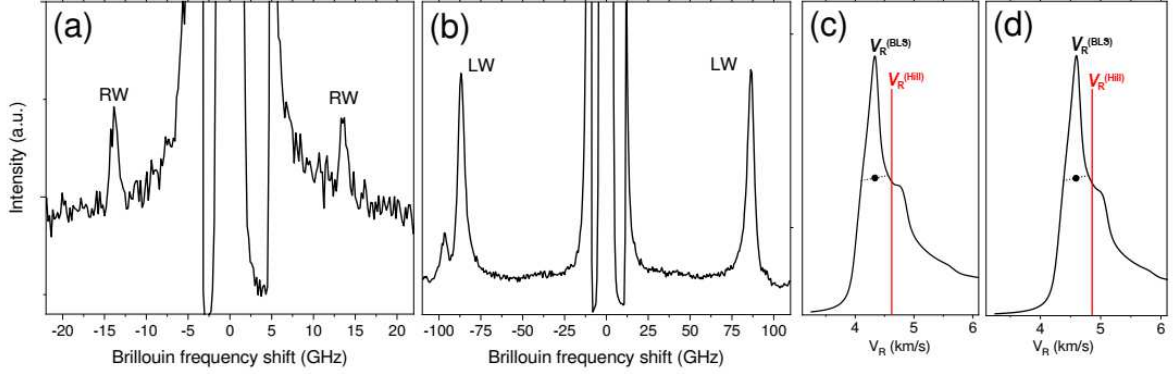


**Figure 3.** (a) BLS spectrum of our  $\gamma$ -Ge<sub>3</sub>N<sub>4</sub> collected in the low-frequency range for the incidence angle of  $\theta=55^\circ$ ; (b) BLS spectrum of our  $\gamma$ -Ge<sub>3</sub>N<sub>4</sub> collected in the wide frequency range for the incidence angle of  $\theta=25^\circ$ . (c, d) Simulated intensity distribution in a BLS peak scattered from a polycrystalline isotropic sample of  $\gamma$ -Ge<sub>3</sub>N<sub>4</sub> in the frequency/velocity range of RWs (black solid lines labelled as  $V_R^{(BLS)}$ ). The simulations were performed for two sets of  $C_{ij}$  calculated (**Table 2**) using the GGA-PBESol- (c) and GGA-PBESol-h functionals (d). Dotted lines indicate FWHM of the simulated peaks and solid circles their middles. Vertical red solid lines, labelled as  $V_R^{(Hill)}$ , indicate velocities of RWs of polycrystalline  $\gamma$ -Ge<sub>3</sub>N<sub>4</sub> calculated using the isotropic moduli  $B_0$  and  $G_0$  derived from the same  $C_{ij}$  applying the Hill approximation.

In order to evaluate the influence of elastic anisotropy on the RW-peak shape in our BLS measurements, we applied a procedure analogous to that developed for the LWs and TWs [57]. We modelled the BLS peak shape in the relevant frequency/velocity range (**Figures 3c-d**) in two steps: (1) we derived the appearance-frequency histogram for frequencies of the sound waves propagating along all directions of the surface delimiting the semi-infinite single-crystalline medium of  $\gamma$ -Ge<sub>3</sub>N<sub>4</sub> with a particular crystallographic orientation. (2) We summed all such histograms derived for all (uniformly distributed) crystallographic orientations of the semi-infinite single-crystalline medium of  $\gamma$ -Ge<sub>3</sub>N<sub>4</sub>. The resulting histogram represented contribution of randomly oriented grains in an infinitely large polycrystalline texture-free sample to the RW-peak intensity. In the model, we used our theoretical  $C_{ij}$  obtained for the PBESol functional in combination with both standard- and hard PAW pseudopotentials. The former functional provided the highest Zener ratio  $A$  while the second one provided  $B_0$  and  $G_0$  (**Table 2**) best matching those from our LU experiments (**Table 1**). In order to model the BLS peak shape, we convoluted the resulting histogram with the Gaussian distribution whose width was equal to the spectrometer resolution at the corresponding frequency. This was realised through an imaginary part of the RW frequency: For any frequency  $f_B$  in the considered region (**Figure 3a**), the complex frequency was represented as  $f_{B,I} = f_B + i \cdot f_B/100$ . The modelled profiles of the RW-peaks are shown in **Figures 3c-d**, where the frequency scale is converted to the sound-velocity scale in order to compare with the velocity  $V_R^{(Hill)}$  calculated using the isotropic  $B_0$  and  $G_0$  derived applying the Hill approximation [36]. As follows from the comparison, position of the modelled RW peak, defined as middle of its full-width-at-half-maximum (FWHM), provides  $V_R^{(BLS)}$  below  $V_R^{(Hill)}$ . Interestingly, the difference  $\delta V_R = V_R^{(Hill)} - V_R^{(BLS)}$  is similar to the difference in the  $V_R$  values in our LU- and BLS measurements. Moreover,  $\delta V_R / V_R^{(Hill)}$

increases with increasing  $A$  and the change rate is considerable: When  $A$  increases from 1.92 to 2.08,  $\delta V_R/V_R^{(\text{Hill})}$  increases from 5.5% to 6.2%. Thus, the experimental difference in the  $V_R$  values of  $\sim 10\%$  can be attributed, at least partially, to the asymmetry of the BLS peak collected from an isotropic polycrystalline sample of  $\gamma\text{-Ge}_3\text{N}_4$ . Because first-principles density functional calculations were reported to underestimate the value of  $A$  [53, 56], the true anisotropy of  $\gamma\text{-Ge}_3\text{N}_4$  can be even stronger and the ratio  $\delta V_R/V_R^{(\text{Hill})}$  can approach that from the LU- and BLS measurements.

Finally, we collected BLS spectra in a wide frequency range and a strong peak with the frequency  $f_{L,0}=86.42(1)$  GHz, due to the LWs, was detected (**Figure 3b**).  $V_{L,0}$  associated with this peak is related to the Brillouin frequency according to the well-known equation:

$$f_{L,0} = V_{L,0} \cdot 2 \cdot n / \lambda_0 \quad (5)$$

where  $n$  is the refractive index of the sample material. Applying **Equation 5**, we obtained  $n \cdot V_{L,0}=22.99(3)$  km/s. Using  $V_{L,p}=9.2(3)$  km/s from our LU measurements and omitting any correction (e.g. due to the elastic anisotropy) we found  $n=2.5(1)$ . In contrast to the RWs, application of the above described corrections due to the elastic anisotropy didn't significantly change the recovered  $n$ : As already mentioned above, BLS peaks of LWs from polycrystalline texture-free samples of elastically anisotropic cubic solids are asymmetric. For  $A>1$ , their centres of mass (or middles of FWHM) shift to higher frequencies/velocities, when compared with the  $V_L$  derived using the Hill approximation [57], and approach  $V_{L(110)}$ :

$$V_{L(110)} = \sqrt{\frac{C_{11}+C_{12}+2C_{44}}{2\rho}} \quad (6)$$

Substituting the theoretical  $C_{ij}$  of  $\gamma\text{-Ge}_3\text{N}_4$ , calculated using either the PBEsol or PBEsol-h functional (**Table 2**), we obtained  $V_{L(110)}=8.67$  km/s or  $V_{L(110)}=9.14$  km/s, respectively. The corresponding theoretical  $B_0$  and  $G_0$ , substituted in **Equation 2**, led to  $V_{L,0} = 8.33$  km/s and  $V_{L,0}=8.84$  km/s, respectively. Thus, the BLS-peak asymmetry should result in an overestimation of the LW velocity by 4.1% and 3.3%, respectively. Applying the latter value, we corrected the product  $n \cdot V_{L,0}$  from our BLS measurement to 22.23(3) km/s. Taking  $V_{L,0}=9.3(4)$  km/s from our LU measurements, we determined the refractive index of  $\gamma\text{-Ge}_3\text{N}_4$  to be  $n=2.4(1)$  at  $\lambda=532$  nm. This experimental value is very similar to our theoretical  $n=2.46$  derived from the dependence  $n(\lambda)$  calculated in the wavelength region of visible light (**Figure 4**). **Figure 4** also shows the wavelength dependent absorption coefficient of  $\gamma\text{-Ge}_3\text{N}_4$ ,  $\kappa(\lambda)$ , which predicts transparency of  $\gamma\text{-Ge}_3\text{N}_4$  at  $\lambda > 360$  nm corresponding to the photon energy  $h \cdot \nu=3.44$  eV. The latter agrees well with the spectroscopically measured band gap of  $\gamma\text{-Ge}_3\text{N}_4$  of  $E_g=3.65(5)$  eV, confirmed experimentally to be direct [4].

Thus, our measurements and calculations provided a very high refractive index of  $\gamma\text{-Ge}_3\text{N}_4$  similar to that of diamond and gallium nitride (GaN) reported to be  $n_{\text{diamond}}=2.42$  [58] and  $n_{\text{GaN}}=2.37$  [59], respectively. This result makes  $\gamma\text{-Ge}_3\text{N}_4$  interesting for advanced optical applications where a high refractive index combined with high hardness, thermal stability in air, and a possibility of machining using diamond tools is required.

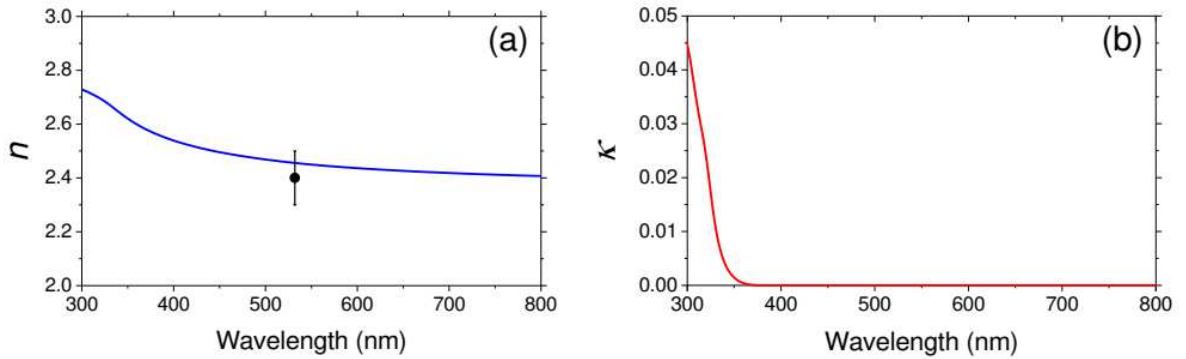


**Figure 4.** Wavelength dependences of (a) refractive index,  $n(\lambda)$ , and (b) absorption coefficient,  $\kappa(\lambda)$ , of  $\gamma\text{-Ge}_3\text{N}_4$ . The theoretical dependences (solid lines) were calculated using the HSE06 hybrid functional. Solid circle shows our experimental  $n$  at  $\lambda=532$  nm, obtained from the combined LU- and BLS measurements.

## 4 Conclusions

In this work, we investigated elastic properties of  $\gamma$ -Ge<sub>3</sub>N<sub>4</sub> experimentally, using the techniques of laser ultrasonics and Brillouin light scattering, and theoretically, using the first-principles density functional calculations. We measured velocities of the RWs and LWs in our low-porosity polycrystalline sample and derived its isotropic elastic moduli  $B_p=304(43)$  GPa and  $G_p=179(6)$  GPa. Applying the Hashin-Shtrikman approach, we obtained  $B_0=322(44)$  GPa and  $G_0=188(7)$  GPa for the dense polycrystalline  $\gamma$ -Ge<sub>3</sub>N<sub>4</sub>. Here, the significant error in  $B_0$  is explained by the low amplitude of the LW-signals in our LU measurements. Nevertheless, it agrees, within the experimental uncertainties, with the  $B_0=295(5)$  GPa obtained from the EOS measured upon quasihydrostatic compression [1]. Both the previous and the present first-principles calculations underestimated  $B_0$  while the GGA-PBEsol functional with the hard PAW potential showed the least deviation from the experiment.

Our experimental  $G_0$  exceeds by  $\sim 1.5$  times the previous experimental value derived from NIT. This difference appears to be caused by the higher oxygen-content in the earlier examined sample but a contribution of porosity cannot be excluded. The calculated  $G_0$  values were mostly underestimated but much less significant than the  $B_0$ . However, the  $G_0$  values of 186(10) GPa and 192(10) GPa obtained from our calculations based on the hard PAW potential in combination with the GGA-PBEsol- and HSE06 functionals, respectively, agreed with our measurements. Comparison of the  $V_{R,0}$  measured using the LU- and BLS techniques confirmed the theoretically-predicted elastic anisotropy of  $\gamma$ -Ge<sub>3</sub>N<sub>4</sub> with  $A>1$ . The anisotropy led to the asymmetric RW peaks in our BLS measurements resulting in the  $V_{R,0}$  underestimated by  $\sim 10\%$ . Such difference in the RW velocities, obtained using the two techniques, can potentially be used to evaluate elastic anisotropy of cubic solids available as powders or polycrystalline bodies only. Here, the main challenge is obtaining of high-quality BLS-peaks with well-defined shapes. Combining our LU- and BLS results for the LWs, we determined refractive index of the dense  $\gamma$ -Ge<sub>3</sub>N<sub>4</sub> to be  $n=2.4(1)$ . This value ranks  $\gamma$ -Ge<sub>3</sub>N<sub>4</sub> in the class of very-high-refractive-index materials transparent for visible light, such as diamond, GaN or TiO<sub>2</sub> having anatase structure.

## Acknowledgments

This work has been carried out within the framework of the EUROfusion Consortium and has received funding from the Euratom research and training programme 2014-2018 and 2019-2020 under grant agreement No 633053. The views and opinions expressed herein do not necessarily reflect those of the European Commission. The multi-anvil apparatus of Laboratoire Magmas et Volcans is financially supported by the INSU-CNRS and the French Government Laboratory of Excellence initiative n°ANR-10-LABX-0006, the Région Auvergne, and the European Regional Development Fund (ClerVolc contribution number xx). Partial support of the the French National Research Agency (ANR, France) through the grant No. ANR-18-CE42-0017 is also acknowledged.

## References

1. Somayazulu, M. S., Leinenweber, K., Hubert, H., McMillan, P. F. & Wolf, G. H. 2000. High pressure - high temperature synthesis of spinel Ge<sub>3</sub>N<sub>4</sub>. In *Science and Technology of High Pressure, Proceedings of AIRAPT-17* (eds. M. Manghnani, W. J. Nellis & M. Nicol), pp. 663-666. Honolulu, Hawaii, USA, Universities Press, Hyderabad, India.
2. Leinenweber, K., O'Keeffe, M., Somayazulu, M., Hubert, H., McMillan, P. F. & Wolf, G. H. 1999. Synthesis and structure refinement of the spinel,  $\gamma$ -Ge<sub>3</sub>N<sub>4</sub>. *Chem. Eur. J.* **5**, 3076-3078. (doi 10.1002/(SICI)1521-3765(19991001)5:10%3C3076::AID-CHEM3076%3E3.0.CO;2-D)
3. Serghiou, G., Miehe, G., Tschauer, O., Zerr, A. & Bohler, R. 1999. Synthesis of a cubic Ge<sub>3</sub>N<sub>4</sub> phase at high pressures and temperatures. *J. Chem. Phys.* **111**, 4659-4662. (doi 10.1063/1.479227)
4. Feldbach, E., Zerr, A., Museur, L., Kitaura, M., Manthilake, G., Tessier, F., Krasnenko, V. & Kanaev, A. 2021. Electronic band transitions in  $\gamma$ -Ge<sub>3</sub>N<sub>4</sub>. *Electron. Mater. Lett.* **17**, 315-323. (doi 10.1007/s13391-021-00291-y)

5. Boyko, T. D., Hunt, A., Zerr, A. & Moewes, A. 2013. Electronic structure of spinel-type nitride compounds  $\text{Si}_3\text{N}_4$ ,  $\text{Ge}_3\text{N}_4$ , and  $\text{Sn}_3\text{N}_4$  with tuneable band gaps: Application to light emitting diodes. *Phys. Rev. Lett.* **111**, 097402. (doi 10.1103/PhysRevLett.111.097402)
6. Nishiyama, N., Langer, J., Sakai, T., Kojima, Y., Holzheid, A., Gaida, N. A., Kulik, E., Hirao, N., Kawaguchi, S. I., Irifune, T., et al. 2019. Phase relations in silicon and germanium nitrides up to 98GPa and 2400 degrees C. *J. Am. Ceram. Soc.* **102**, 2195-2202. (doi 10.1111/jace.16063)
7. He, H., Sekine, T., Kobayashi, T. & Kimoto, K. 2001. Phase transformation of germanium nitride ( $\text{Ge}_3\text{N}_4$ ) under shock wave compression. *J. Appl. Phys.* **90**, 4403-4406. (doi 10.1063/1.1407851)
8. Ruddlesden, S. N. & Popper, P. 1958. On the crystal structures of the nitrides of silicon and germanium. *Acta Cryst.* **11**, 465-468. (doi 10.1107/S0365110X58001304)
9. Shemkunas, M. P., Petuskey, W. T., Chizmeshya, A. V. G., Leinenweber, K. & Wolf, G. H. 2004. Hardness, elasticity, and fracture toughness of polycrystalline spinel germanium nitride and tin nitride. *J. Mater. Res.* **19**, 1392-1399. (doi 10.1557/JMR.2004.0186)
10. Zerr, A., Eschnauer, H. & Kny, E. 2012. Hard materials. In *Ullmann's Encyclopedia of Industrial Chemistry, Electronic Release* (ed. B. Elvers), pp. 1-21. Weinheim/Germany, Wiley-VCH. (doi 10.1002/14356007.a12\_603.pub2)
11. Dong, J. J., Deslippe, J., Sankey, O. F., Soignard, E. & McMillan, P. F. 2003. Theoretical study of the ternary spinel nitride system  $\text{Si}_3\text{N}_4$ - $\text{Ge}_3\text{N}_4$ . *Phys. Rev. B* **67**, 094104. (doi 10.1103/PhysRevB.67.094104)
12. Boyko, T. D., Bailey, E., Moewes, A. & McMillan, P. F. 2010. Class of tunable wide band gap semiconductors  $\gamma$ - $(\text{Ge}_x\text{Si}_{1-x})_3\text{N}_4$ . *Phys. Rev. B* **81**, 155207. (doi 10.1103/PhysRevB.81.155207)
13. Boyko, T. D. & Moewes, A. 2016. The hardness of group 14 spinel nitrides revisited. *Journal of the Ceramic Society of Japan* **124**, 1063-1066. (doi 10.2109/jcersj2.16097)
14. Zerr, A. 2008. Comments on "Hardness, elasticity, and fracture toughness of polycrystalline spinel germanium nitride and tin nitride," by MP Shemkunas, WT Petuskey, AVG Chizmeshya, K. Leinenweber, and GH Wolf *J. Mater. Res.* **19**, 1392 (2004) : Reestablishing of elastic moduli for  $\gamma$ - $\text{Ge}_3\text{N}_4$ . *J. Mater. Res.* **23**, 3273-3274. (doi 10.1557/jmr.2008.0405)
15. Luo, Y. S., Cang, Y. P. & Chen, D. 2014. Determination of the finite-temperature anisotropic elastic and thermal properties of  $\text{Ge}_3\text{N}_4$ : A first-principles study. *Comput. Condens. Matter* **1**, 1-7. (doi 10.1016/j.cocom.2014.08.001)
16. Xiang, H. M., Feng, Z. H., Li, Z. P. & Zhou, Y. C. 2018. Theoretical predicted high-thermal-conductivity cubic  $\text{Si}_3\text{N}_4$  and  $\text{Ge}_3\text{N}_4$ : promising substrate materials for high-power electronic devices. *Sci. Rep.* **8**, 14374. (doi 10.1038/s41598-018-32739-x)
17. Dong, J. J., Sankey, O. F., Deb, S. K., Wolf, G. & McMillan, P. F. 2000. Theoretical study of  $\beta$ - $\text{Ge}_3\text{N}_4$  and its high-pressure spinel  $\gamma$  phase. *Phys. Rev. B* **61**, 11979-11992. (doi 10.1103/PhysRevB.61.11979)
18. Hu, H. & Peslherbe, G. H. 2021. Accurate mechanical and electronic properties of spinel nitrides from density functional theory. *J. Phys. Chem. C* **125**, 8927-8937. (doi 10.1021/acs.jpcc.0c09896)
19. Ching, W. Y., Mo, S.-D., Tanaka, I. & Yoshiya, M. 2001. Prediction of spinel structure and properties of single and double nitrides. *Phys. Rev. B* **63**, 064102. (doi 10.1103/PhysRevB.63.064102)
20. Lowther, J. E. 2000. High-pressure phases and structural bonding of  $\text{Ge}_3\text{N}_4$ . *Phys. Rev. B* **62**, 5-8. (doi 10.1103/PhysRevB.62.5)
21. Teter, D. M. 1998. Computational alchemy: the search for new superhard materials. *MRS Bull.* **23**, 22-27. (doi 10.1557/S0883769400031420)
22. Zerr, A., Riedel, R., Sekine, T., Lowther, J. E., Ching, W. Y. & Tanaka, I. 2006. Recent advances in new hard high-pressure nitrides. *Adv. Mater.* **18**, 2933-2948. (doi 10.1002/adma.200501872)
23. Morkoc, H., Strite, S., Gao, G. B., Lin, M. E., Sverdlov, B. & Burns, M. 1994. Large band-gap SiC, III-V nitride, and II-VI ZnSe-based semiconductor device technologies. *J. Appl. Phys.* **76**, 1363-1398. (doi 10.1063/1.358463)
24. Viswanath, A. K., Lee, J. I., Kim, D., Lee, C. R. & Leem, J. Y. 1998. Exciton-phonon interactions, exciton binding energy, and their importance in the realization of room-temperature semiconductor lasers based on GaN. *Phys. Rev. B* **58**, 16333-16339. (doi 10.1103/PhysRevB.58.16333)
25. Museur, L., Zerr, A. & Kanaev, A. 2016. Photoluminescence and electronic transitions in cubic silicon nitride. *Sci. Rep.* **6**, 18523. (doi 10.1038/srep18523)

26. Sickafus, K. E., Grimes, R. W., Valdez, J. A., Cleave, A., Tang, M., Ishimaru, M., Corish, S. M., Stanek, C. R. & Uberuaga, B. P. 2007. Radiation-induced amorphization resistance and radiation tolerance in structurally related oxides. *Nat. Mater.* **6**, 217-223. (doi 10.1038/nmat1842)
27. Sickafus, K. E., Minervini, L., Grimes, R. W., Valdez, J. A., Ishimaru, M., Li, F., McClellan, K. J. & Hartmann, T. 2000. Radiation tolerance of complex oxides. *Science* **289**, 748-751. (doi 10.1126/science.289.5480.748)
28. Zerr, A., Chigarev, N., Brenner, R., Dzivenko, D. A. & Gusev, V. 2010. Elastic moduli of hard c-Zr<sub>3</sub>N<sub>4</sub> from laser ultrasonic measurements. *Phys. Status Solidi-Rapid Res. Lett.* **4**, 353-355. (doi 10.1002/pssr.201004345)
29. Zerr, A., Chigarev, N., Brinza, O., Nikitin, S. M., Lomonosov, A. M. & Gusev, V. 2012. Elastic moduli of η-Ta<sub>2</sub>N<sub>3</sub>, a tough self-healing material, via laser ultrasonics. *Phys. Status Solidi - Rapid Research Letters* **6**, 484-486 (doi 10.1002/pssr.201206419)
30. Dzivenko, D. A., Zerr, A., Schweitzer, E., Göken, M., Boehler, R. & Riedel, R. 2007. Elastic moduli and hardness of c-Zr<sub>2.86</sub>(N<sub>0.88</sub>O<sub>0.12</sub>)<sub>4</sub> having Th<sub>3</sub>P<sub>4</sub>-type structure. *Appl. Phys. Lett.* **90**, 191910. (doi 10.1063/1.2738373)
31. Friedrich, A., Winkler, B., Bayarjargal, L., Arellano, E. A. J., Morgenroth, W., Biehler, J., Schroder, F., Yan, J. Y. & Clark, S. M. 2010. In situ observation of the reaction of tantalum with nitrogen in a laser heated diamond anvil cell. *J. Alloys Comp.* **502**, 5-12. (doi 10.1016/j.jallcom.2010.04.113)
32. Hammersley, A. P., Svensson, S. O., Hanfland, M., Fitch, A. N. & Hausermann, D. 1996. Two-dimensional detector software: From real detector to idealised image or two-theta scan. *High Pressure Res.* **14**, 235-248. (doi 10.1080/08957959608201408)
33. Deb, S. K., Dong, J., Hubert, H., McMillan, P. F. & Sankey, O. F. 2000. The Raman spectra of the hexagonal and cubic (spinel) forms of Ge<sub>3</sub>N<sub>4</sub>: an experimental and theoretical study. *Solid State Comm.* **114**, 137-142. (doi 10.1016/S0038-1098(00)00017-X)
34. Schwarz, M., Miehe, G., Zerr, A., Kroke, E., Poe, B. T., Fuess, H., Rubie, D. C., & Riedel, R. 2000. Spinel-Si<sub>3</sub>N<sub>4</sub>: Multi-anvil press synthesis and structural refinement. *Adv. Mater.* **12**, 883-887 (doi: 10.1002/1521-4095(200006)12:12<883::AID-ADMA883>3.0.CO;2-C)
35. Nishiyama, N., Ishikawa, R., Ohfuji, H., Marquardt, H., Kurnosov, A., Taniguchi, T., Kim, B.-N., Yoshida, H., Masuno, A., Bednarcik, J., Kulik, E., Ikuhara, Y., Wakai, F., & Irifune, T. 2017. Transparent polycrystalline cubic silicon nitride. *Sci. Rep.* **7**, 44755. (doi 10.1038/srep44755)
36. Hill, R. 1952. The elastic behaviour of a crystalline aggregate. *Proc. Phys. Soc. A* **65**, 349-354. (doi 10.1088/0370-1298/65/5/307)
37. Sandercock, J. R. 1970. Brillouin scattering study of SbSI using a double-passed, stabilised scanning interferometer. *Opt. Commun.* **2**, 73-76. (doi 10.1016/0030-4018(70)90047-7)
38. Hillebrands, B. 1999. Progress in multipass tandem Fabry-Perot interferometry: I. A fully automated, easy to use, self-aligning spectrometer with increased stability and flexibility. *Rev. Sci. Instrum.* **70**, 1589-1598. (doi 10.1063/1.1149637)
39. Kresse, G. & Joubert, D. 1999. From ultrasoft pseudopotentials to the projector augmented-wave method. *Phys. Rev. B* **59**, 1758-1775. (doi 10.1103/PhysRevB.59.1758)
40. Perdew, J. P., Ruzsinszky, A., Csonka, G. I., Vydrov, O. A., Scuseria, G. E., Constantin, L. A., Zhou, X. L. & Burke, K. 2008. Restoring the density-gradient expansion for exchange in solids and surfaces. *Phys. Rev. Lett.* **100**, 136406. (doi 10.1103/PhysRevLett.100.136406)
41. Perdew, J. P., Burke, K. & Ernzerhof, M. 1996. Generalized gradient approximation made simple. *Phys. Rev. Lett.* **77**, 3865-3868. (doi 10.1103/PhysRevLett.77.3865)
42. Kresse, G. & Furthmüller, J. 1996. Efficient iterative schemes for ab initio total-energy calculations using a plane-wave basis set. *Phys. Rev. B* **54**, 11169-11186. (doi 10.1103/PhysRevB.54.11169)
43. Perdew, J. P., Tao, J. M., Staroverov, V. N. & Scuseria, G. E. 2004. Meta-generalized gradient approximation: Explanation of a realistic nonempirical density functional. *J. Chem. Phys.* **120**, 6898-6911. (doi 10.1063/1.1665298)
44. Le Page, Y. & Saxe, P. 2002. Symmetry-general least-squares extraction of elastic data for strained materials from ab initio calculations of stress. *Phys. Rev. B* **65**, 104104. (doi 10.1103/PhysRevB.65.104104)

45. Design, M. 1998-2021. Medea. (San Diego, CA, Materials Design, Inc.)
46. Krukau, A. V., Vydrov, O. A., Izmaylov, A. F. & Scuseria, G. E. 2006. Influence of the exchange screening parameter on the performance of screened hybrid functionals. *J. Chem. Phys.* **125**, 224106. (doi 10.1063/1.2404663)
47. Ouahrani, T., Daouli, A., Badawi, M., Bendaoudi, L., Morales-García, Á., & Errandonea, D. 2022. Understanding the thermodynamic, dynamic, bonding, and electrocatalytic properties of low-dimensional MgPSe<sub>3</sub>. *Dalton Trans.* **51**, 9689-9698. (doi 10.1039/D2DT01194H)
48. Ouahrani, T., Garg, A. B., Rao, R., Rodríguez-Hernández, P., Muñoz, A., Badawi, M., & Errandonea, D. 2022. High-pressure properties of wolframite-type ScNbO<sub>4</sub>. *J. Phys. Chem. C* **126**, 4664–4676. (doi 10.1021/acs.jpcc.1c10483)
49. Heyd, J., Peralta, J. E., Scuseria, G. E. & Martin, R. L. 2005. Energy band gaps and lattice parameters evaluated with the Heyd-Scuseria-Ernzerhof screened hybrid functional. *J. Chem. Phys.* **123**, 174101. (doi 10.1063/1.2085170)
50. Landau, L. D. & Lifshitz, E. M. 1959. *Theory of elasticity*. London, Pergamon Press.
51. Hashin, Z. & Shtrikman, S. 1962. On some variational principles in anisotropic and nonhomogeneous elasticity. *J. Mech. Phys. Solids* **10**, 335-342. (doi 10.1016/0022-5096(62)90004-2)
52. Marquardt, H., Speziale, S., Gleason, A., Sinogeikin, S., Kantor, I. & Prakapenka, V. B. 2013. Brillouin scattering and x-ray diffraction of solid argon to 65 GPa and 700 K: Shear strength of argon at HP/HT. *J. Appl. Phys.* **114**, 093517. (doi 10.1063/1.4820578)
53. Raetz, S., Kuriakose, M., Djemia, P., Nikitin, S. M., Chigarev, N., Tournat, V., Bulou, A., Lomonosov, A., Gusev, V. E. & Zerr, A. 2019. Elastic anisotropy and single-crystal moduli of solid argon up to 64 GPa from time-domain Brillouin scattering. *Phys. Rev. B* **99**, 224102. (doi 10.1103/PhysRevB.99.224102)
54. Bourguille, J., Brinza, O., Tetard, F., Nikitin, S. & Zerr, A. 2015. Elastic moduli and hardness of  $\eta$ -Ta<sub>2</sub>N<sub>3</sub> from nanoindentation measurements. *EPL* **111**, 18006. (doi 10.1209/0295-5075/111/18006)
55. Zerr, A., Kempf, M., Schwarz, M., Kroke, E., Göken, M. & Riedel, R. 2002. Elastic moduli and hardness of cubic silicon nitride. *J. Am. Ceram. Soc.* **85**, 86-90. (doi 10.1111/j.1151-2916.2002.tb00044.x)
56. Kuriakose, M., Raetz, S., Hu, Q. M., Nikitin, S. M., Chigarev, N., Tournat, V., Bulou, A., Lomonosov, A., Djemia, P., Gusev, V. E., et al. 2017. Longitudinal sound velocities, elastic anisotropy, and phase transition of high-pressure cubic H<sub>2</sub>O ice to 82 GPa. *Phys. Rev. B* **96**, 134122. (doi 10.1103/PhysRevB.96.134122)
57. Xu, F., Djemia, P., Belliard, L., Huang, H., Perrin, B. & Zerr, A. 2021. Influence of elastic anisotropy on measured sound velocities and elastic moduli of polycrystalline cubic solids. *J. Appl. Phys.* **130**, 035903. (doi 10.1063/5.0053372)
58. Wilks, J. & Wilks, E. 1991. *Properties and Applications of Diamond*, 1st. ed. Oxford, Butterworth-Heinemann; 525 p.
59. Yu, G., Wang, G., Ishikawa, H., Umeno, M., Soga, T., Egawa, T., Watanabe, J. & Jimbo, T. 1997. Optical properties of wurtzite structure GaN on sapphire around fundamental absorption edge (0.78-4.77 eV) by spectroscopic ellipsometry and the optical transmission method. *Appl. Phys. Lett.* **70**, 3209-3211. (doi 10.1063/1.119157)

## **Additional Information**

### **Data Accessibility**

All data are given in the paper.

### **Authors' Contributions**

### **Competing Interests**

We have no competing interests.